




Ultrafast four-dimensional imaging of cardiac mechanical wave propagation with sparse optoacoustic sensing

Çağla Özsoy^{a,b,c,1} , Ali Özbek^{a,b,c,1}, Michael Reiss^{a,b,c}, Xosé Luís Deán-Ben^{a,b,c}, and Daniel Razansky^{a,b,c,2}

^aInstitute of Pharmacology and Toxicology, Faculty of Medicine, University of Zürich, Zürich 8057, Switzerland; ^bInstitute for Biomedical Engineering, Faculty of Medicine, University of Zürich, Zürich 8057, Switzerland; and ^cInstitute for Biomedical Engineering, Department of Information Technology and Electrical Engineering, ETH Zürich, Zürich 8093, Switzerland

Edited by Igor R. Efimov, George Washington University, Washington, D.C., and accepted by Editorial Board Member John A. Rogers September 21, 2021 (received for review February 28, 2021)

Propagation of electromechanical waves in excitable heart muscles follows complex spatiotemporal patterns holding the key to understanding life-threatening arrhythmias and other cardiac conditions. Accurate volumetric mapping of cardiac wave propagation is currently hampered by fast heart motion, particularly in small model organisms. Here we demonstrate that ultrafast four-dimensional imaging of cardiac mechanical wave propagation in entire beating murine heart can be accomplished by sparse optoacoustic sensing with high contrast, ~115- μ m spatial and submillisecond temporal resolution. We extract accurate dispersion and phase velocity maps of the cardiac waves and reveal vortex-like patterns associated with mechanical phase singularities that occur during arrhythmic events induced via burst ventricular electric stimulation. The newly introduced cardiac mapping approach is a bold step toward deciphering the complex mechanisms underlying cardiac arrhythmias and enabling precise therapeutic interventions.

imaging ultrafast phenomena | optoacoustic tomography | photoacoustics | ultrafast volumetric imaging | Langendorff

The first observation of irregular spikes in electrocardiogram (ECG) signals in the early 1900s (1) has fostered vast research efforts to unravel the fundamental mechanisms underlying cardiac arrhythmias (2–4). The information encoded in ECG signals corresponds to the integrated electrical activity of cardiac cells. Point-by-point ECG mapping combined with modeling of tissue electrical properties has enabled localizing the onset and propagation paths of irregular electric signaling in the heart (5). Electrocardiographic imaging further combined multiple ECG body-surface readings with full-body X-ray computed tomography (CT) or MRI scans to map the electrical activity on the epicardial heart surface (6, 7). While delivering excellent contrast for imaging cardiac anatomy and blood flow (8–10), the temporal resolution of CT and MRI is insufficient for three-dimensional (3D) visualization of transient nonperiodic events in the heart. Models linking the electrophysiology of single cells to the propagation of electric signals in cardiac muscles have subsequently been developed, yet complete depiction of the entire heart motion in real-time and 3D remains challenging without employing cardiac gating (11). Progress in ultrasound (US) imaging recently enabled attaining millisecond-scale temporal resolutions, leading to major advances in characterization of the cardiac motion. Particularly, visualization of electromechanical and shear waves in the heart was possible with ultrafast US (12, 13). In parallel, development of optical probes of transmembrane voltage (14, 15) and intracellular calcium (16, 17) has provided unprecedented insights into cardiovascular physiology and the mechanisms of electrical activity (18, 19). A combination between US and optical mapping has further enabled the multimodal characterization of scroll waves in an isolated Langendorff pig heart model (20), a pivotal step toward better understanding of the heart rhythm disorders.

Despite major technical advances, the spatiotemporal resolution and penetration of the currently available cardiac imaging modalities hinders the transmural visualization of fast electromechanical phenomena across the entire beating heart, particularly in small model organisms. The effective spatiotemporal resolution of ultrafast volumetric US is ultimately limited by the need for compounding multiple plane-wave transmissions in order to achieve sufficient image contrast (21, 22). While offering important benefits, such as fast response times (23) and accurate spatial mapping capacity (24), the strong photon scattering in biological tissues fundamentally confines optical mapping to surface-weighted two-dimensional (2D) observations (25, 26), whereas motion artifacts associated with the myocardial contractions further lead to out-of-focus artifacts complicating action potential readings (18, 27–29). Other common impediments of extrinsic cardiac labeling approaches include phototoxicity (30), photobleaching (31), and nonphysiological changes in the heart (32).

Recent progress in the development of optoacoustic (OA) tomography methods have attained a unique combination

Significance

Propagation of electromechanical waves in excitable heart muscles follows complex spatiotemporal patterns holding the key to understanding life-threatening arrhythmias. Despite recent progress, there is a lack of cardiac imaging methods capable of transmural visualization of fast electromechanical phenomena across the beating heart. Here we introduce a sparse optoacoustic sensing technique for ultrafast four-dimensional imaging of cardiac mechanical wave propagation in the entire beating murine heart with high contrast and sub-millisecond temporal resolution. We extract accurate dispersion and phase velocity maps of the cardiac waves and reveal vortex-like patterns associated with mechanical phase singularities that occur during arrhythmic events induced via ventricular stimulation. Our cardiac mapping approach is a bold step toward deciphering the complex mechanisms underlying cardiac arrhythmias.

Author contributions: Ç.Ö., X.L.D.-B., and D.R. designed research; Ç.Ö., A.Ö., M.R., and X.L.D.-B. performed research; Ç.Ö. and A.Ö. analyzed data; Ç.Ö., A.Ö., X.L.D.-B., and D.R. wrote the paper; A.Ö. developed the inversion algorithms; and X.L.D.-B. and D.R. supervised research.

The authors declare no competing interest.

This article is a PNAS Direct Submission. I.R.E. is a guest editor invited by the Editorial Board.

Published under the PNAS license.

¹Ç.Ö. and A.Ö. contributed equally to this work.

²To whom correspondence may be addressed. Email: daniel.razansky@uzh.ch.

This article contains supporting information online at <http://www.pnas.org/lookup/suppl/doi:10.1073/pnas.2103979118/-DCSupplemental>.

Published November 3, 2021.

between fast volumetric imaging speed, deep-tissue penetration, and high molecular sensitivity (26, 33–35), making this modality particularly attractive for studying cardiac function. Whole-heart OA imaging at 50-Hz volumetric frame rates was demonstrated for the Langendorff-perfused model (36) as well as in vivo by capturing bulk perfusion of optical contrast agents (37, 38). Healing of infarcted myocardium in models of coronary occlusion and c-kit mutants has further been studied using this approach (39), highlighting its unique capacity for multi-parametric characterization of morphological and functional changes in murine models of myocardial infarction.

Yet, accurate mapping of microscopic tissue deformations in a rapidly beating murine heart implies 3D imaging at significantly faster frame rates on a submillisecond temporal resolution scale (39, 40). Here, we demonstrate that ultrafast four-dimensional imaging of cardiac mechanical wave propagation in the entire beating murine heart can be accomplished using sparse OA sensing (SOS) of volumetric cardiac motion. Our approach is based on a rapid compressed acquisition of OA responses from randomized subsets of US detection channels followed by iterative reconstruction of the entire image sequence with infimal convolution of the total variation (ICTV) functional. In this way, we were able to efficiently delineate the

multiscale spatiotemporal information encoded in the volumetric heart motion with high-contrast, $\sim 115\text{-}\mu\text{m}$ spatial, and sub-millisecond temporal resolution.

Results

Ultrafast Imaging of the Heart with SOS. A dedicated SOS platform was designed to optimally record four-dimensional tomographic information from entire isolated murine hearts with ultrahigh (submillisecond) temporal resolution (Fig. 1A, *Materials and Methods*, and *SI Appendix, Fig. S1 and Note 1*). The key condition for achieving robust whole-heart imaging performance is uniform illumination of the heart surface, which was achieved here by guiding the excitation light from multiple directions using a custom-made seven-arm fiber bundle (*SI Appendix, Fig. S2 and Note 2*). The spherical matrix array transducer used for detecting the generated signals was further designed with a broad (150°) angular coverage to achieve uniform sensitivity and nearly isotropic, $\sim 115\text{-}\mu\text{m}$ spatial resolution (*SI Appendix, Fig. S3 and Note 3*) across the imaged heart volume (41). The firmware of the data acquisition system (DAQ), which is normally capable of handling simultaneous acquisition from all the 512 channels of the spherical array at 100-Hz

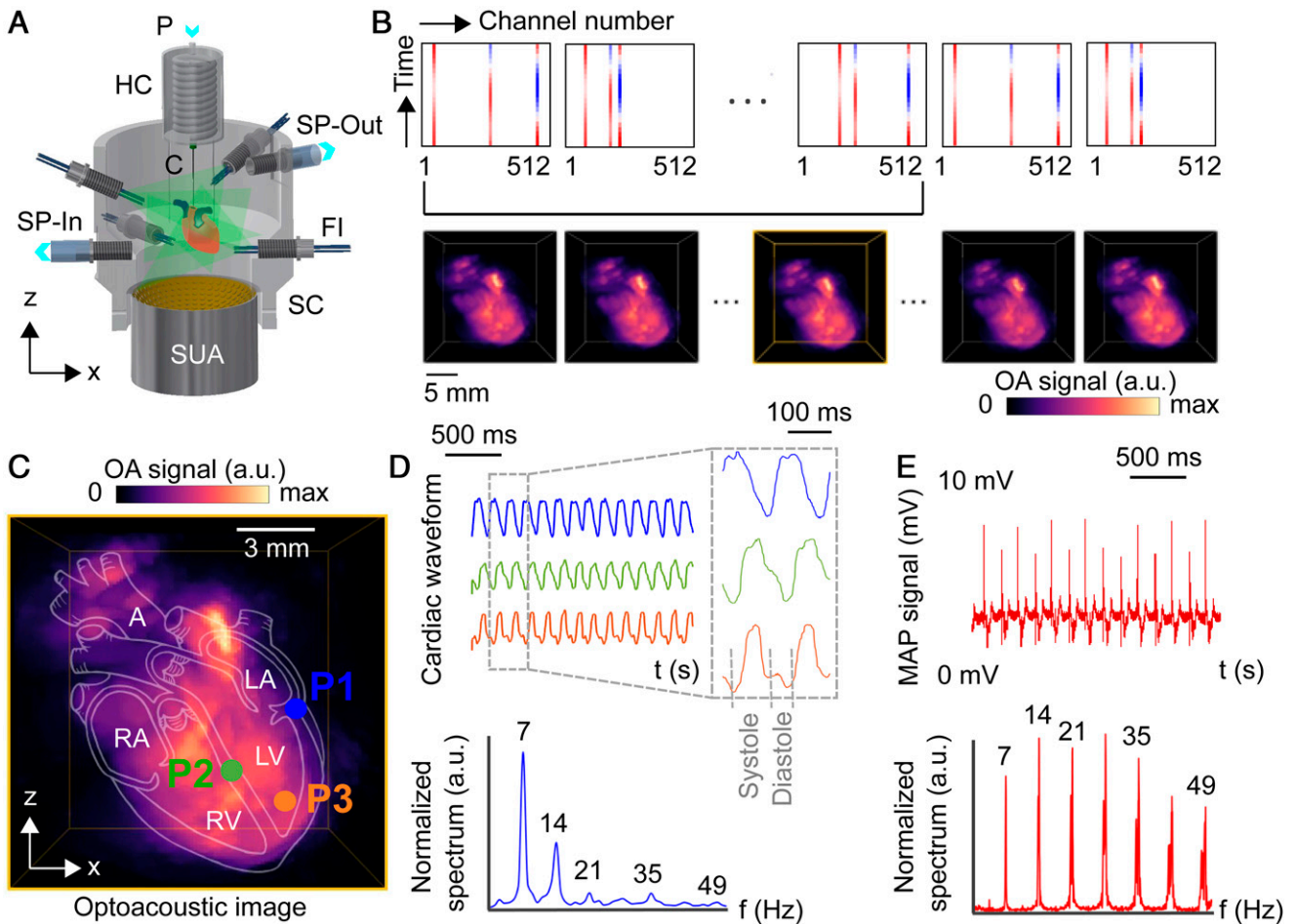


Fig. 1. The SOS platform for ultrafast four-dimensional imaging of cardiac mechanical wave propagation. (A) Schematics of the experimental setup used for volumetric SOS of murine Langendorff-isolated heart. P: perfusion, HC: heating coil, C: cannula, SP-Out: superfusion out, SP-In: superfusion in, FI: fiber input, SC: sample chamber, and SUA: spherical US array. (B) The sparse acquisition and reconstruction scheme. Lines indicate the sparsely selected channels from the entire 512-channel signal sinograms. The SOS algorithm employs a moving-window acquisition scheme by reconstructing a sequence of n volumetric image frames for every n consecutive acquisitions, from which the central frame is taken as an output for every time instant (frame). (Scale bar, 5 mm.) (C) Representative volumetric image of the heart (central frame in B) where major heart structures, aorta (A), left ventricle (LV), right ventricle (RV), right atrium (RA), and left atrium (LA), are labeled. (Scale bar, 3 mm.) (D) Temporal signal profiles for the selected points (P1, P2, and P3) indicated in C and their average Fourier transform. Individual heart cycles are shown in the *Inset*. (E) Simultaneous MAP recording and its corresponding Fourier transform.

frame rate, was redesigned to enable compressed data acquisition from a small subset of channels for every laser pulse with up to 1600-Hz frame rate (i.e., submillisecond temporal resolution). For this, the acquisition was split into $m = 8$ sequentially recorded groups, each consisting of $n = 64$ randomized array elements (Fig. 1B). Image reconstruction using ICTV-based iterative inversion was simultaneously performed for eight consecutive frames corresponding to full recording from all the 512 array channels. Note that SOS employs a moving window acquisition scheme with the central reconstructed image frame taken as an output for every time instant (frame). We then characterized temporal resolution of SOS under controlled conditions by visualizing propagation of surface waves in water (SI Appendix, Note 4). Wave velocities in the 1-m/s range were readily estimated from the volumetric images taken at 1.4 kHz frame rate (SI Appendix, Fig. S4), thus validating that the method's temporal resolution is sufficient for visualizing cardiac mechanical waves in mice.

Ultrafast SOS imaging was then performed in isolated (Langendorff) heart preparations in which the cardiac cell viability was maintained for up to several hours by delivering oxygen and nutrients through the coronary arteries while preserving the temperature and pH in the physiological range (42). Key anatomical features of the heart can readily be identified in the 3D projection views of the reconstructed SOS images (Fig. 1C). Analysis of the temporal signal profiles further enables accurately discerning the cardiac cycle (Fig. 1D). A closer look into an individual heart cycle (Inset in Fig. 1D) readily reveals delays between the mechanical activation of different regions, evincing the high temporal resolution achieved with the suggested image formation protocol. The average temporal frequency spectra of the selected signals (Fig. 1D) reasonably match that of the simultaneously recorded monophasic action potential (MAP) signals (Fig. 1E), although some differences are well anticipated considering the entirely different (electrical) nature of the MAP recordings.

Visualization of Cardiac Mechanical Wave Propagation via Phase Mapping. Visualization of electromechanical wave propagation was achieved by considering the temporal phase of the acquired SOS image sequence at the fundamental heart beating frequency of 7 Hz (i.e., the first peak in the MAP spectrum in Fig. 1E). The phase was calculated via pixel-based temporal Fourier transform (Materials and Methods). Propagation of the electromechanical wave along the heart surface can clearly be identified via the phase gradient (Fig. 2A, Top). The $\sim 180^\circ$ phase flip between the two ventricles (Fig. 2A, Bottom) is presumably attributed to the lateral heart motion associated with contraction of the heart suspended from the cannula. Note that the phase map corresponding to a propagating wave in a contracting heart is fundamentally different from that corresponding to rigid motion. To illustrate this, we imaged an oscillatory motion induced in an externally vibrated (nonbeating) heart (SI Appendix, Fig. S5). No propagating wave was observed even though the vibration motion did affect the SOS signal amplitude in individual voxels and hence the calculated phase maps. Note also that the wave could only be visualized after placing the heart into solidified agar medium while no reliable mapping was possible in a freely swinging heart solely attached to the cannula (SI Appendix, Fig. S6 and Note 5). Characterization of the mechanical wave propagation through the left ventricle can be achieved by extracting the actual phase velocity from the gradient maps (arrows in Fig. 2B). A single cross-section through the heart phase map (Fig. 2C) indicates that the phase velocity changes associated to wave propagation are superimposed onto those associated to a lateral oscillation of the bulk volume around the point where the heart is attached to the reperfusion cannula (indicated in Fig. 2C). The overall direction of

propagation is from the apex toward the atrium (Movie S1), as expected for a regular heartbeat (43). Phase velocities in the 0.5-m/s range are observed (Fig. 2D), in good agreement with previously reported values (43, 44). When plotted against the frequency of oscillations (Fig. 2E), the phase velocity at selective points on the heart (indicated in Fig. 2D) exhibits a dispersive behavior, which can also be inferred from the noninvasive clinical ECG readings (45). However, direct observations and 4D characterization of cardiac wave dispersion in fast-beating murine hearts is beyond reach for other cardiac imaging modalities that either lack the spatiotemporal resolution or can only deliver images of individual 2D cross-sections or projections in real time. Note that the introduced ICTV-based reconstruction was instrumental for enabling robust visualization and analysis of cardiac wave propagation based on the sparse high-frame rate signal recordings, as evinced by comparison to other known OA image reconstruction techniques that rendered inferior performance (SI Appendix, Fig. S7 and Note 6).

Spatiotemporal Characterization of Ventricular Arrhythmias with SOS. The unique capabilities of the developed SOS approach have been further tested in an arrhythmia model. Ventricular arrhythmia was induced in retrogradely perfused mouse hearts ($n = 15$) via epicardial burst stimulation with bipolar needle electrodes (Fig. 3A). MAP electrodes were further placed at the right atrium and the apex to assess the generated arrhythmic events. The heart beats regularly before stimulation (Movie S2), while irregular beating is transiently induced for several seconds (Movie S3) before the regular MAP signal pattern is eventually recovered (Fig. 3B). Horizontal placement of the heart avoids substantial exposure of the electrodes, optimally positioned tangentially on the epicardium, to the excitation light pulses, hence mitigating the associated artifacts in the reconstructed SOS images. Alternatively, electric field stimulation can be used with electrodes located at a certain distance from the heart (46). Spatiotemporal changes in activation during cardiac tachycardia were analyzed by considering the time-variant signals recorded by SOS for different locations on the heart wall. Irregularities of the heartbeat are clearly detected in the temporal profiles (Fig. 3C), generally matching the patterns observed in the MAP images. Note, however, that while the signal phase has been reported as an effective readout for analyzing the spatiotemporal changes during fibrillation, the amplitude was shown to be a more ambiguous parameter affected by external or physiological factors unrelated to fibrillatory activity (47). Hilbert transform (HT) of each time profile (Fig. 3C) corresponds to the instantaneous phase (14), which can then be plotted against the original profiles to result in the complex phase space plots (Fig. 3D). The instantaneous phase at an arbitrary time point can be calculated as the corresponding angle θ with respect to the horizontal axis in the phase space plot (Fig. 3D).

The phase space plots generally manifest a dispersive trajectory yet looping around a central point, as typically observed during fibrillation events (47). In murine hearts, the dominant frequency of sustained spiral wave reentry has previously been shown to vary within a wide range, from 13.6 Hz up to 38 Hz (48, 49). Our experimental results generally corroborate these findings, further indicating that induction of arrhythmic events and their dominant frequencies largely depend on the position of stimulation electrodes as well as stimulation intensity (49), which was varied between 1 and 10 mA. For instance, temporal evolution of the instantaneous phase maps in a heart featuring a dominant reentry frequency of 40 Hz (calculated via mean voxel spectrum) clearly reveals the singularities around which the phase is rotating (Fig. 3E). Such phase singularities (PS) correspond to the reentrance of activation waves, namely, the stable mechanical scroll waves as well as drifting mechanical filaments in ventricular fibrillation (20) observed due to the

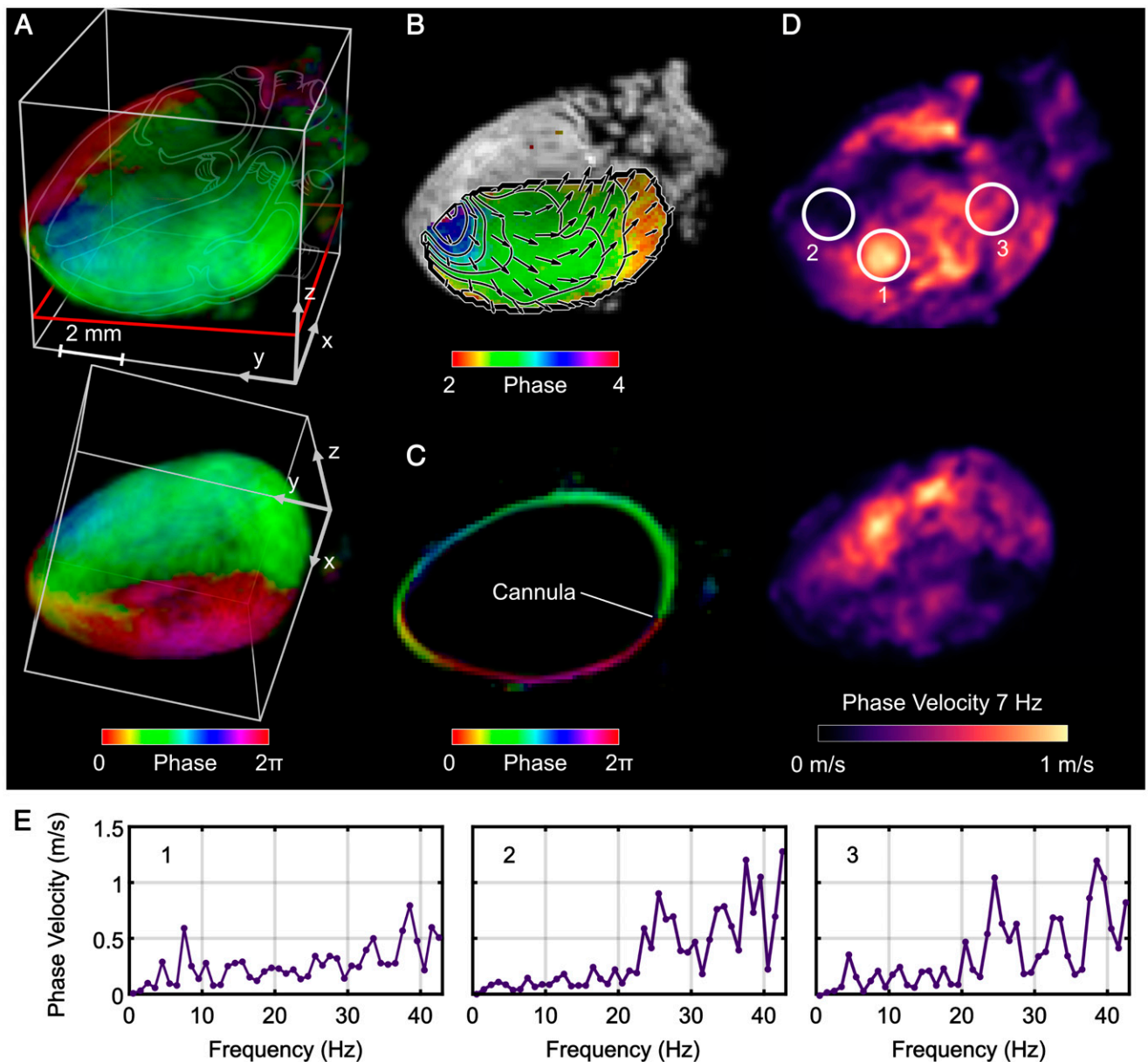


Fig. 2. Visualization of cardiac mechanical wave propagation via phase mapping. (A) Color-coded phase map for the 7-Hz wave component; two 3D views are shown. (Scale bar, 2 mm.) (B) Phase velocity vector in the left ventricle (represented by arrows) as calculated from the gradient of the phase map. The 7-Hz amplitude image of the heart is shown as a grayscale background. (C) Central cross-section through the bottom image volume in A indicated with a red rectangle. (D) Amplitudes of the phase velocities along the heart surface. (E) Phase velocity as a function of frequency for the three points indicated in D.

spontaneous wave splitting or wave breaks (50). These can provide important insights into the mechanisms that sustain cardiac tachycardia and fibrillation. Herein, only PS associated with stable mechanical scroll waves have been shown in a ventricular tachycardia model. Similarly, ventricular fibrillation with drifting spiral wave cores also exhibit narrowband spectra (51) and could potentially be detected with the suggested approach at the corresponding dominant frequency. Lower dominant frequencies in the 10- to 11-Hz range were observed in other hearts (*SI Appendix, Fig. S8*) in which the presence of stimulation electrodes also caused an image artifact in the region where the PS was detected (*SI Appendix, Fig. S8A, Top row*). Note that the lack of PS prior to stimulation indicates that the PS generation during the arrhythmic phase is not ascribed to an image artifact caused by the electrodes. Also, the instantaneous phase maps acquired before attaching the

stimulation electrodes to the ventricle (prestimulus period) were not afflicted with the artifacts (*Top rows in Fig. 3E and SI Appendix, Fig. S8B*), exhibiting the expected wave propagation from the apex to base (*Movie S1*). The PS was then observed during stimulation without any discernible artifacts present in the phase maps of their rhythmical counterparts (*Bottom rows in Fig. 3E and SI Appendix, Fig. S8B*). The temporal evolution of the phase maps before and during electrical (burst) stimulation are further available in the movies accompanying the online version of the manuscript (*Movies S4 and S5*).

To further investigate the dominant frequency phenomenon, we extracted the normalized MAP spectra from respective temporal signals during rhythmical (i.e., prior to stimulation, Fig. 4B) and arrhythmic (i.e., during stimulation, Fig. 4C) periods. Isochronal maps of the heart motion were then composed from the time domain data band-pass filtered between 3 and 53 Hz

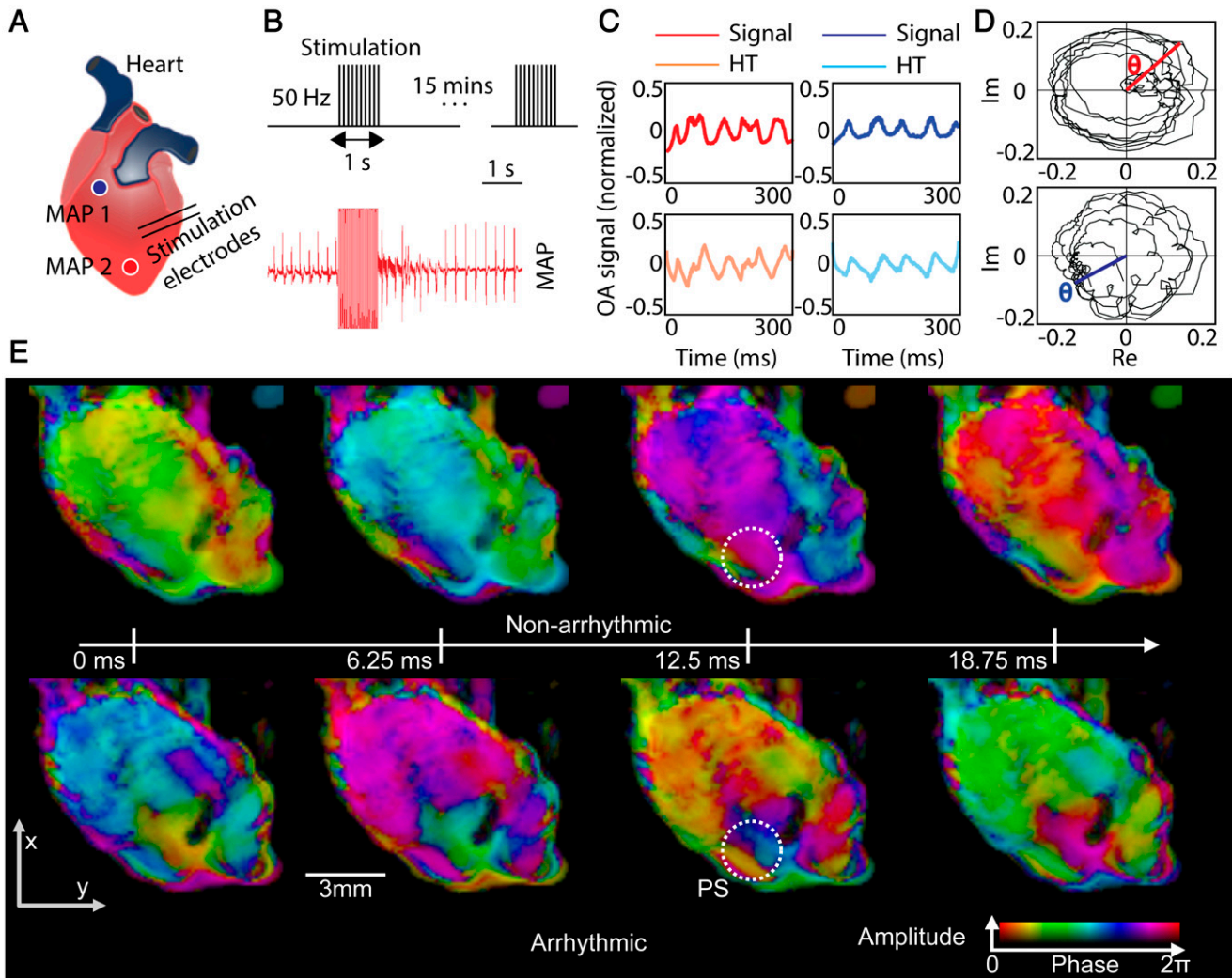


Fig. 3. Spatiotemporal characterization of ventricular arrhythmias with SOS. (A) Schematic drawing of the ventricular arrhythmia model induced via epicardial burst stimulation with bipolar needle electrodes. The electrical stimulation is performed with 50 Hz, 1-s duration bursts, and 15-min intervals to allow for recovery of the cardiac cycle. Positions of the stimulation and MAP electrodes are indicated. (B) Recorded MAP signal during stimulation with an electric burst. (C) Temporal signal profiles of two representative voxels (labeled red and blue in A) along with the corresponding HTs (imaginary parts of the reconstructed signal profiles). (D) Phase space plots demonstrating the relationship between the two temporal signal profiles and their corresponding HTs. (E) Four consecutive instantaneous phase maps demonstrating the nonarrhythmic period of the isolated heart when stimulation was not applied (Top). The respective arrhythmic period (after stimulation) is also shown (Bottom). PS around which the phase rotates is clearly identified in the phase maps filtered with a narrow band-pass filter corresponding to the dominant frequency of 40 Hz. (Scale bar, 3 mm.)

(Fig. 4A). Note that the images were thresholded to exclude the regions outside the heart and the inner ventricular cavity. The isochronal maps depict the wavefront propagation originating in the apex of the heart and traveling toward its top. The normalized mean spectrum across all the image voxels was subsequently extracted (Fig. 4D) and phase maps for the observed peaks in the frequency domain were calculated in a representative cross-section of the heart where PS locations can readily be identified (highlighted in Fig. 4E) up to a dominant frequency of 31 Hz.

PS and Mechanical Filaments inside the Ventricular Wall. An automatic PS detection algorithm was further devised to identify the rotors occurring during ventricular arrhythmias in the right ventricle (Materials and Methods and SI Appendix, Fig. S9). Basically, PS correspond to points with nonzero curl (line integral) of the phase gradient. The detected double PS denoted with black circles are shown for a slice corresponding to the reference vertical position ($z = 0$ mm) along with the phase and phase gradient maps (Fig. 5A). The PS were also computed for

the consecutive cross-sections ($z = 0$ to $z = +0.4$ mm) of the same heart (zoomed in regions shown in Fig. 5B). Mechanical filaments (black curves) connecting between the PS are readily observed inside the ventricular wall (Fig. 5B). Such filaments were also observed within the ventricular wall of a different isolated heart when using modified S1 to S2 electrical stimulation period (Materials and Methods and Fig. 5C). The corresponding temporal signal profiles extracted from a selected voxel during the rhythmic (prestimulation) and arrhythmic (poststimulation) phases clearly evince the arrhythmic activity (Fig. 5D). A video depicting the phase map dynamics during the stimulation period is further available in the online manuscript version (Movie S6). The oscillatory patterns observed at locations distant from the vortex-like wave (i.e., mechanical PS) (Movie S6) can be attributed to paired and unpaired PS (52). While the paired singularities represent colocalized cores of the mechanical and electrical re-entrant waves, the unpaired singularities are associated with the long-range elastic interactions and anisotropy of the active field.

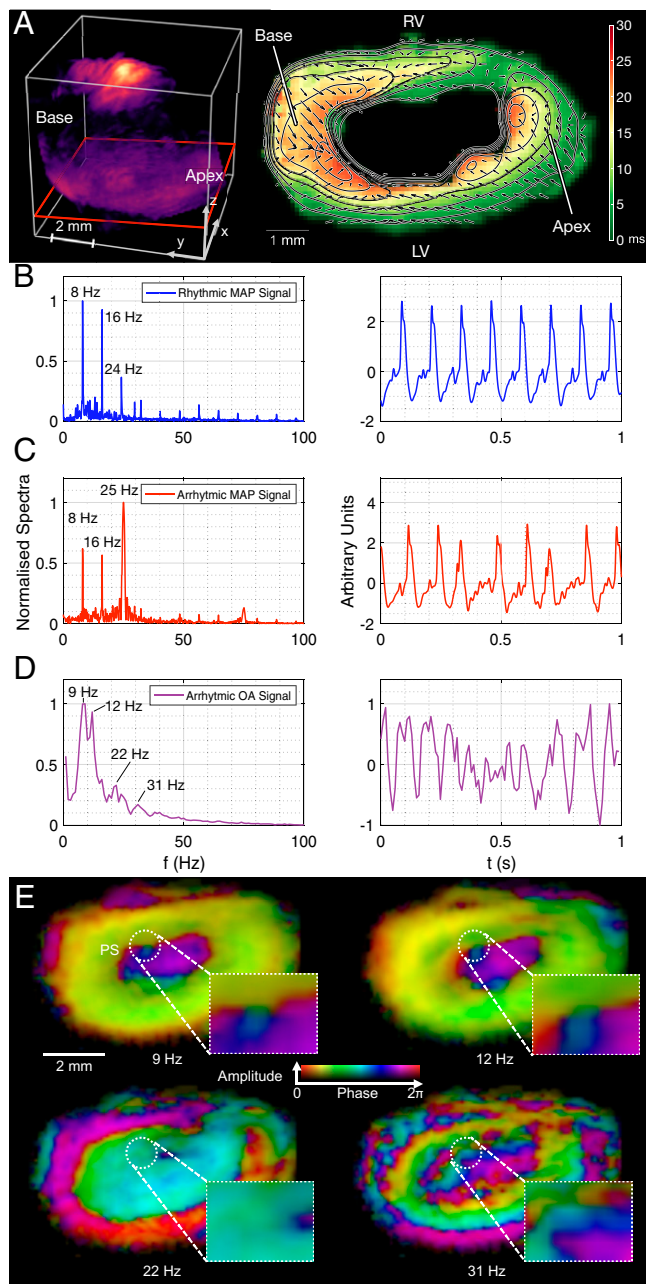


Fig. 4. Frequency analysis of the arrhythmic heart motion. (A) Isochronal map (Right) of the cross-sectional SOS image through the heart ventricle indicated with a red rectangle (Left). Color maps represent the time that it takes for the wavefront to propagate to each point in the image. Arrows depict travel direction of the local wavefront. Major heart structures including left ventricle (LV), right ventricle (RV), apex, and base are labeled. (Scale bar, 1 mm.) (B) Normalized MAP amplitude spectrum (Left) extracted from the prestimulation (rhythmic) period (Right). (C) The corresponding MAP spectrum (Left) for the poststimulation (arrhythmic) phase (Right). (D) Normalized mean SOS voxel spectrum (Left) extracted from mean temporal signal (Right) during the arrhythmic phase. (E) Phase maps corresponding to each of the four peak frequencies shown in D. The magnified region containing the PS is shown in the *Insets* for each corresponding frequency. (Scale bar, 2 mm.)

Discussion

The ability to visualize cardiac mechanical waves in the entire heart at $\sim 115\text{-}\mu\text{m}$ spatial and submillisecond temporal resolution scales can massively advance our understanding of the

cardiac function in health and disease. At present, no imaging method provides sufficient temporal resolution for truly four-dimensional imaging with adequate contrast and spatial resolution to reliably characterize the cardiac wave propagation in murine models. While compounding of multiple plane-wave excitations is required to form images with ultrafast US, the introduced SOS method offers unique capabilities for imaging the entire Langendorff-perfused heart via simultaneous illumination of the heart surface with a nanosecond duration pulse of light (single-shot excitation), thus facilitating ultrafast volumetric OA imaging at kilohertz frame rates. We were able to extract accurate dispersion and phase-velocity maps of the cardiac waves in murine hearts and reveal vortex-like patterns associated with mechanical PS that occur during arrhythmic events induced via burst ventricular electric stimulation.

The phase-maps discontinuities stemming from the signal subsampling may represent potential limitation of the suggested approach. Future studies will aim at generating more uniform phase maps employing DAQs with accelerated data transfer rates (currently limited to 1 Gbit/s), thus averting subsampling of the tomographic data. The visible light wavelengths used in the experiments provided a good trade-off between optical contrast, chiefly arising from absorption by myoglobin and other chromophores present in perfused hearts and deep-tissue penetration not compromised by the presence of whole blood. The superior spatial resolution and contrast of SOS with respect to pulse-echo US modalities is also associated with the speckle-free nature of tomographic OA imaging (53). Indeed, accurate SOS reconstructions are highly dependent upon broad tomographic angular coverage, which was facilitated with the spherical arrangement of elements of the transducer array employed in this study. Note, however, that SOS solely relies on temporal phase estimations at a given frequency of the signal intensity fluctuations, namely, no information on the amplitude or direction of the local deformations is readily available. As opposed to ultrafast US imaging methods that rely on speckle tracking to provide tissue deformation maps (54, 55), the speckle-free nature of OA imaging imposes limitations when it comes to direct 3D motion tracking of smooth surfaces. Thereby, a quantitative relationship between the temporal phase and directional deformation (strain tensor) could not be extracted. However, the gradient of the calculated phase maps clearly indicates the presence of a propagating cardiac mechanical wave.

The developed SOS reconstruction methodology based on the ICTV regularization was essential for rendering sequences of 3D images with sufficient quality to reliably extract wave propagation data from the sparse signal acquisitions. Similar methods were previously attempted for compressed sensing applications in MRI in which the image could be considered piecewise constant, both spatially and temporally (56). However, the ICTV-based method introduced herein further allows striking a fine balance between temporal and spatial regularization of the multiscale SOS data while also adapting the reconstruction algorithm to the specific content of typical heart images, a difficult task for the conventional back-projection- or compressed-sensing-based reconstruction algorithms (SI Appendix, Fig. S7). TV-based compressed sensing methods have previously been used to reconstruct sparse data by treating space and time as equal dimensions, which resulted in image blurring due to rapid motion and an overall decrease in spatiotemporal resolution and image quality (40). In contrast, the ICTV method mitigates these shortcomings by splitting the TV regularizer into two independent spatial and temporal parts and weighing them optimally as part of the optimization algorithm. In this way, recovery of fast signal changes was greatly facilitated while preserving the spatial features in regions where changes were slow. This approach is particularly suitable for imaging the heart dynamics in which majority of the

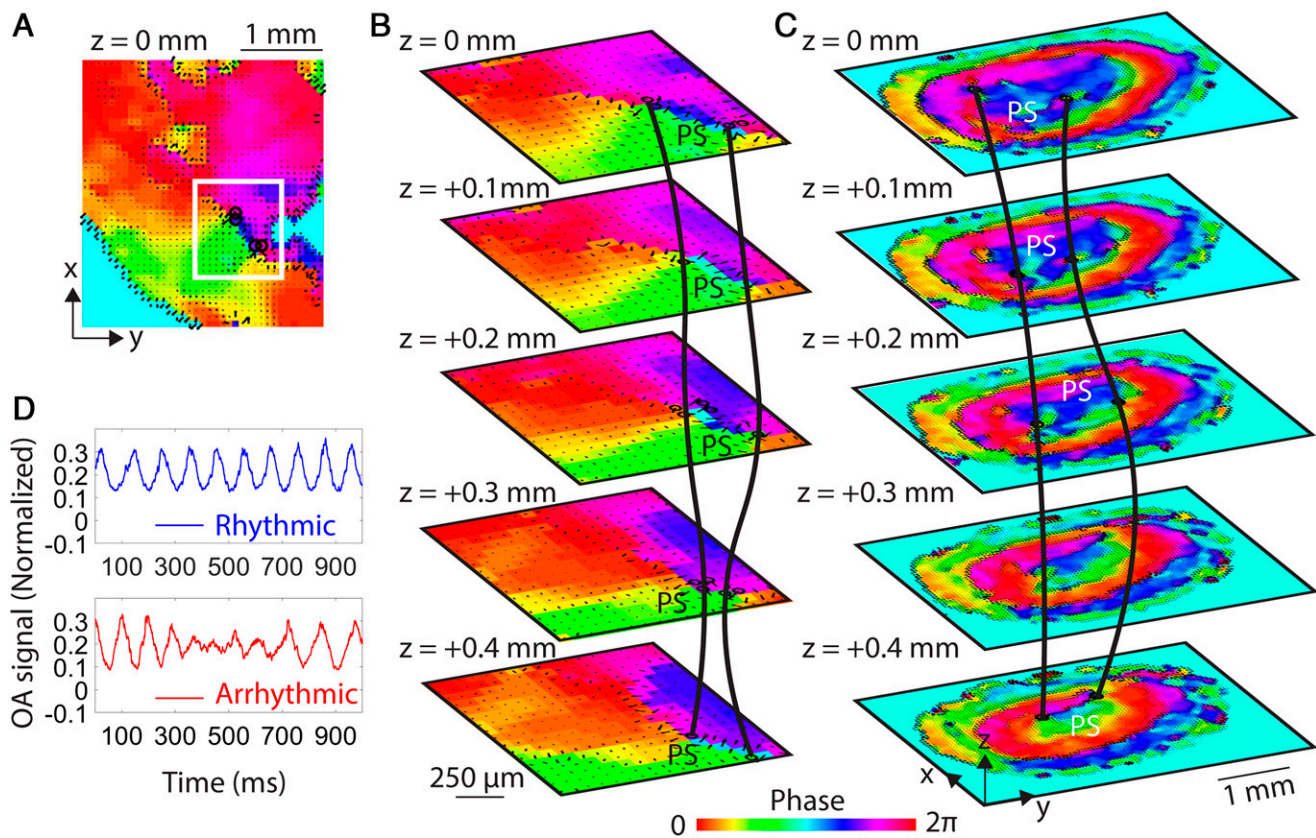


Fig. 5. Automatic PS detection and mechanical filaments inside the ventricular wall. (A) A double PS detected in a heart that was subjected to the burst stimulation sequence. (B) 3D image stack around the area indicated with the white rectangle in A. The filament (black line) connecting the PS in each cross-section is shown. (C) Automatically detected PS in a heart that was subjected to programmed electrical stimulation (S1 to S2). The filament connecting the PS in each cross-section is similarly indicated with a black curve. Phase maps were filtered with a narrow band-pass filter corresponding to the dominant frequencies of 40 Hz (B) and 26 Hz (C) prior to automatic PS detection. (D) Rhythmic (blue) and arrhythmic (red) temporal profiles of the SOS signals from a selected voxel of the heart during the pre- and poststimulation phases.

reconstructed volume corresponds to slowly moving structures superimposed onto a rapid motion induced by propagating mechanical waves. A large sequence of 3D images can then be reconstructed from a relatively small amount of data, thus making it possible to perform long recordings covering the entire duration of the arrhythmic events. Additional improvements in the algorithm implementation (e.g., by efficiently transferring data between the Graphics Processing Unit [GPU] and main memory) may reduce computational costs, thus further expediting reconstructions currently benchmarking at about 1 min per frame.

The multifiber illumination arrangement was also essential to efficiently cover the entire heart volume with a single excitation light pulse, especially considering the limited penetration of light at 532 nm. In this context, excitation at longer wavelengths in the near-infrared range is preferable for visualizing internal heart structures, particularly if isolated hearts from larger animal models are of interest. This may for instance enable mapping the propagation of shear waves through the heart valves, which have been shown to contain information on the heart muscle stiffness (57, 58). Development of new laser sources operating in the near-infrared spectral window at kilohertz repetition rates and millijoules per-pulse energy is yet imperative for enabling such implementations and can significantly advance the capabilities of SOS. Near-infrared excitation is also crucial when it comes to visualizing cardiac dynamics in vivo in the presence of strong background absorption by whole blood (38, 39).

Even though electrical and mechanical activity in the heart have fundamentally different natures, the two are known to be coupled at the cellular level with the synchronization altered under disease conditions (13). For instance, the mechanical deformation of the heart incorporates a local active stress component oriented in the fiber direction induced by the propagating action potentials but also has a long-range effect, which can only be distinguished by solving the inverse mechano-electrical problem (59). It has further been shown that electrical and mechanical PS coexist in vortex-like scroll waves generated during ventricular fibrillation or tachycardia (20). We observed oscillatory wave patterns that occur at locations far from the vortex-like waves (mechanical PS). A similar phenomenon has recently been reported (52) whereby the paired (electromechanical) PS alongside with the unpaired PS formed due to the spatiotemporal inhomogeneities in the strain fields. Electrical measurements could thus potentially be employed in order to accurately discern the two types of PS. However, the current SOS system implementation is only capable of providing dimensionless electrical measurements with no independent validation of the 3D mechanical wave motion possible.

As opposed to optical microscopy and diffuse tomography, the SOS method is generally not hindered by intense light scattering and thus can render high-resolution images deep from living tissues. On the other hand, SOS is performed with single-shot excitation (i.e., no compounding of multiple plane wave excitation is required), which in turn leads to a higher temporal resolution than is possible with plane-wave compounding in

US. However, SOS potentially holds another key advantage as it relies on the rich optical absorption contrast. While the current study was performed with single-wavelength excitation, multispectral imaging may enable mapping of additional parameters such as oxygenation of myoglobin whose spectra differ substantially in oxygenated and deoxygenated states (60). Given the large versatility of intrinsic optical absorption contrast and extrinsic agents, the SOS method could be then explored for multiparametric characterization of the cardiac function across multiple spatial and temporal scales (61). In particular, it has been recently demonstrated that neural activity associated with variations of intracellular calcium concentration in murine and vertebrate brains expressing genetically encoded calcium indicators can be sensed with functional OA neuro-tomography (62–64). An analogous approach can potentially be applied to study the mechanisms underlying electromechanical coupling in the heart with SOS, provided that suitable absorption-based labels are developed for sensing of electrical signaling in the heart (e.g., based on voltage or calcium indicators). Yet, in order to achieve multispectral imaging capabilities at kilohertz frame rates, the pulsed-laser technology needs to further evolve to provide wavelength tuning capabilities with microsecond speed while maintaining sufficiently high per pulse energy levels and pulse repetition frequency.

All in all, the ultrafast four-dimensional imaging approach introduced in this work is a powerful tool for studying electromechanical propagation phenomena in the small-sized rapidly beating murine heart at multiple spatial and temporal scales. It is therefore anticipated to facilitate studies into fundamental mechanisms underlying cardiac arrhythmias, thus benefitting the diagnosis and treatment of life-threatening arrhythmias and other clinical conditions.

Materials and Methods

Langendorff Preparation. A total of $n = 24$ female CD1 mice ranging between 8 and 9 wk of age were used in the experiments. The Langendorff preparation was performed by overdosing the animal with a mixture of ketamine (150 mg/kg) and xylazine (10 mg/kg) to harvest the heart. After confirming the absence of pain reflex by pinching the paw, the heart was surgically removed from the body. The excised heart was then placed on an ice-cold Petri dish containing Tyrode's solution. Lungs and excess of fat tissue around the heart were carefully removed with forceps and surgical scissors. The ascending aorta was identified and cannulated under a stereo microscopy with a 21-gauge cannula, which was initially perfused with the Tyrode's (42) solution and fixed with a 4–0 black-braided silk suture (Resorba GmbH) (SI Appendix, Fig. S1 and Note 1). All the animal experiments were carried out in accordance with the Swiss Federal Act on Animal Protection and were approved by the Cantonal Veterinary Office Zurich.

The SOS Imaging Setup. SOS experiments were accomplished with a custom-made water-filled chamber containing an agar base that accommodates the Langendorff-isolated heart model, the excitation light delivery system, and the spherical matrix detection array for volumetric data acquisition (Fig. 1A). The inlet and outlet of the superfusion system are further inserted into the chamber. The spherical array was fixed at the bottom and sealed with an O-ring to prevent leakage of the superfusion Tyrode's solution. The array is composed of 512 piezocomposite elements distributed on its spherical active surface over a 150° angle. The array has a 7-MHz central frequency and $\sim 80\%$ detection bandwidth providing $10 \times 10 \times 10 \text{ mm}^3$ effective field of view with approximately isotropic resolution of $\sim 115 \mu\text{m}$ around the center of the spherical geometry (SI Appendix, Fig. S3 and Note 3). Illumination of the heart was performed with a frequency-doubled Q-switched diode laser providing 10-ns duration light pulses at 532 nm (EdgeWave GmbH). The per-pulse energy and the pulse repetition frequency of the laser were set to 4 mJ and 1.6 kHz, respectively. The laser beam was guided to uniformly illuminate the heart surface with a custom-made fiber bundle consisting of 21 individual multimode fibers with 0.5 numerical aperture and 600- μm core diameter (ThorLabs, Inc.). The fibers were randomly distributed in seven output ferrules that were inserted into a central 5-mm diameter aperture of the array and into six apertures of the chamber arranged at angular elevations of 37° and 5.7° with respect to the central axis of the array (Fig. 1A). All output ferrules of the

bundle were directed toward the center of the spherical array geometry and sealed with O-rings to prevent leakage of the superfusion Tyrode's solution. The total energy per pulse measured at the output of the fiber bundle was $\sim 1 \text{ mJ}/\text{cm}^2$.

Data Acquisition. The individual time-resolved OA signals recorded by the array's elements were digitized at 24 megasamples per second with a custom-made parallel DAQ (Falkenstein Mikrosysteme GmbH). An imaging rate of 1.6 kHz was enabled by acquiring signals only from a subset of elements for each laser pulse. Specifically, eight groups with randomly distributed elements were considered with the partial data acquired sequentially over subsequent laser pulses (Fig. 1B). Signal acquisition was synchronized with the Q-switch output of the laser via an external signal generator. Each time-resolved signal consisted of 256 samples acquired with a 20.089- μs delay following the laser emission corresponding to the minimal distance between the imaged object and the active detection surface. In each experiment, 16,000 consecutive image frames were recorded, corresponding to a total acquisition time of ~ 10 s. The acquired data were transmitted to a personal computer via Ethernet at a rate of 419 Mbit/s.

The SOS Inversion Procedure. Three-dimensional images were reconstructed from the sparsely acquired OA signals with a model-based iterative ICTV approach. Specifically, discretization of the forward OA signal propagation model was performed to derive an algebraic equation in which a pressure vector \mathbf{p}_i representing the sparsely recorded signals for the i -th frame is expressed via

$$\mathbf{p}_i = \mathbf{C}_i \mathbf{A} \mathbf{h}_i, \quad [1]$$

where \mathbf{h}_i is the absorbed light energy distribution at a grid of points enclosing the imaged object, expressed in a vector form, for the i -th frame. \mathbf{A} is the model matrix mapping optical absorption to pressure signals at the detection locations whose calculation is described elsewhere (65). \mathbf{C}_i is the subsampling matrix corresponding to the active elements for the i -th frame. Considering a sequence of l frames, the corresponding algebraic models can be combined via

$$\mathbf{p} = \mathbf{C}_{\text{tot}} \mathbf{h}, \quad [2]$$

where $\mathbf{p} = (p_1, p_2, \dots, p_n)^T$, $\mathbf{C} = \text{diag}(C_1, C_2, \dots, C_n)$, and $\mathbf{A}_{\text{tot}} = \mathbf{I}_n \otimes \mathbf{A}$, \mathbf{I}_n being the n by n identity matrix and $\mathbf{h} = (h_1, h_2, \dots, h_n)^T$. The matrix \mathbf{C} corresponding to randomly selected channels is very likely to fulfill the restricted isometry property required for accurate compressed-sensing based reconstruction. Thereby, the inversion problem to simultaneously reconstruct the entire sequence of image frames can be defined as

$$\mathbf{h} = \underset{\mathbf{h}}{\text{argmin}} \left\{ \frac{1}{2} \|\mathbf{p}_m - \mathbf{C}_{\text{tot}} \mathbf{h}\|_2^2 + \lambda \cdot \text{ICTV}(\mathbf{h}) \right\}, \quad [3]$$

where $\frac{1}{2} \|\mathbf{p}_m - \mathbf{C}_{\text{tot}} \mathbf{h}\|_2^2$ is the fidelity term and $\text{ICTV}(\mathbf{h})$ is the regularization term corresponding to

$$\text{ICTV}(\mathbf{h}) = \underset{\mathbf{v}}{\text{argmin}} \{ \text{TV}_s(\mathbf{u} - \mathbf{v}) + \gamma \cdot \text{TV}_t(\mathbf{v}) \}, \quad [4]$$

$$\text{TV}_s(\mathbf{u}) = \sqrt{ \left(\frac{\delta u}{\delta x} \right)^2 + \left(\frac{\delta u}{\delta y} \right)^2 + \left(\frac{\delta u}{\delta z} \right)^2 + \kappa^2 \left(\frac{\delta u}{\delta t} \right)^2 }, \quad [5]$$

$$\text{TV}_t(\mathbf{h}) = \sqrt{ \kappa^2 \left(\frac{\delta u}{\delta x} \right)^2 + \kappa^2 \left(\frac{\delta u}{\delta y} \right)^2 + \kappa^2 \left(\frac{\delta u}{\delta z} \right)^2 + \left(\frac{\delta u}{\delta t} \right)^2 }. \quad [6]$$

The term $0 < \kappa < 1$ is a weighing factor that enables optimally accounting for the spatial and temporal sparsity of the image sequence. A proximal descent based fast iterative shrinkage and thresholding algorithm was used to split the minimization problem in Eqs. 4 through 6 into two parts. Just a few iterations involving matrix–vector multiplications are sufficient for the fidelity part in Eq. 3 (66), which is the dominant processing power requirement in the optimization problem. The second part of the reconstruction involves approximating the proximal of the ICTV, which is sufficient for convergence (67). The primal–dual hybrid gradient algorithm developed by Chambolle and Pock (68) was used for this purpose, which alternates proximal descent steps in primal and dual spaces of the convex problem.

The model–matrix and vector multiplications as well as the computation of the ICTV proximal were accelerated using a custom OpenCL code running on an NVIDIA GeForce GTX TITAN X graphics card. The remaining computations were performed on an Intel i7-7700K central processing unit. Due to memory limitations of the GPU, the reconstruction was implemented as a moving window of eight frames, in which only the middle two frames were considered in each step.

Phase Velocity Measurements and Isochronal Maps. Phase mapping was performed offline following data acquisition and image reconstruction. Fourier analysis was used to extract the relevant frequency information. Given that the heart beats in a regular and periodic manner, fundamental and harmonic frequencies of the heartbeat were clearly identified in the Fourier spectra of each image voxel. More prominent peaks were detected at the voxels close to the interfaces between the heart wall and the surrounding fluid, where the reconstructed signal values change from zero to a maximum value. While more-reliable phase values were obtained when the phase map extraction was limited to the outer wall boundary (Fig. 2C), it was also possible to extract phase maps also from the inner heart regions (Fig. 4A). Phase maps were created by considering voxel-dependent phase in the Fourier transform of the volumetric SOS images for the relevant frequencies. These maps were visualized in red–green–blue format, in which the image hue represents the phase while brightness stands for the amplitude. The frequency-dependent phase velocity was then estimated from the gradient of the calculated-phases maps.

Isochronal maps of the mechanical wave propagation were created by calculating the time that it takes for the voxels in the SOS image sequence to attain a certain reference intensity value (Fig. 4A). For this, the reference time point is selected to be at the beginning of systolic phase while the reference voxel is taken at the apex of the heart. The raw data were band-pass filtered between 3 and 53 Hz before processing. Only pixels for which the signal intensity was above a certain threshold were considered, whereas other voxels were not displayed. Color maps represent the time that it takes for the wavefront to propagate to every point in the image. Arrows depict the local wavefront travel direction, which is estimated from the gradient of the isochronal map. The length of the arrows is proportional to the inverse of gradient's magnitude. Hence, the direction and magnitude of the arrows represent velocity vector of the wavefront propagation.

Model of Ventricular Arrhythmia. Ventricular arrhythmia was induced using either burst stimulation or a programmed electrical stimulation (S1 to S2) protocol (69). For the former, electrical stimulation (1 to 10 mA, 2 ms) was applied via bipolar needle electrodes in the left ventricle of the isolated heart. The distance between the two electrodes was ~5 mm (Fig. 3A). A burst stimulation at 50 Hz for a 1-s duration (50 pulses) was applied epicardially as described elsewhere (70). An electrical stimulator (SYS-A365R, World Precision Instruments) and a function/waveform generator (33220A, Agilent) were employed for this purpose. For the programmed electrical stimulation protocol (SI Appendix, Fig. S10), 20 100-ms-duration S1 stimuli followed by 20 extra S2 stimuli were applied. The extra stimuli initiated with a 60-ms cycle length, gradually decreasing toward 20 ms with 2-ms decrements. The electrical stimulus protocol was programmed using an open-source pulse train generator (Pulse Pal, Sanworks LLC). As opposed to healthy hearts, arrhythmic hearts ($n = 15$) were horizontally placed onto the supporting solidified agar base in the imaging chamber using an L-shaped (i.e., prebent) 21-gauge cannula. Under these conditions, the heart could still contract while being perfused with the Tyrode's solution and mechanically supported by the agar medium to minimize swinging motion. The horizontal orientation further facilitated epicardial placement of the stimulation electrodes, thus avoiding artifacts in the reconstructed images due to light absorption by the metallic electrodes. To measure the local electrical activity in the myocardium (71), MAPs were measured. Unlike what is typically done for in vivo measurements, the MAP electrodes were placed at the right atrium and the apex (SI Appendix, Fig. S11 and Note 7) with the bipolar electrogram recorded using a DAQ (PowerLab 26T ADInstruments) and a differential amplifier (DP-311, Warner Instruments). The

amplifier's gain, high-pass, and low-pass frequencies were set to 10 Hz, 100 Hz, and 1 KHz, respectively. MAP signals were recorded prior, during, and after electrical stimulation and subsequently analyzed by the LabChart software (ADInstruments). Single-sided amplitude spectra of MAP signals were extracted in MATLAB using the Fast Fourier function covering both the prestimulation (rhythmic) and stimulated (arrhythmic) phases (Fig. 4 B and C). The rhythmic heartbeat spectrum consists of the 8-Hz peak frequency as well as the second and third harmonic frequencies at 16 and 24 Hz. The burst stimulation causing arrhythmia is seen in the spectrum as the most prominent peak at 25 Hz.

Arrhythmia Detection Using Dominant Frequency Analysis. The phase maps used for the detection of arrhythmic events were calculated following the dominant frequency analysis (72, 73), which extracts the power spectral density from the Fast Fourier Transform of each voxel of the reconstructed volumetric image sequence. Average voxel values for the entire image sequence were subtracted for reliable phase calculation (14). Arrhythmias in the mouse heart are spread across a wide range of dominant frequencies (48, 49, 74). Accordingly, the peak frequencies were determined in the amplitude spectrum extracted from voxels on the ventricular wall located in the vicinity of the electrically stimulated region. A narrow band-pass filter corresponding to each dominant frequency was subsequently applied to the reconstructed image sequences to minimize the effect of cardiac activity unrelated to the arrhythmic event, which has been previously implemented to stabilize PS in atrial fibrillation (75). An analytical signal was then calculated (MATLAB function `hilbert()`), from which the HT (18, 20, 47) was extracted (imaginary part of the analytic signal). The instantaneous phase (between $-\pi$ and $+\pi$) value was defined for each voxel as the argument of the time-resolved analytic signal with the real part being the original reconstructed OA signal and imaginary part its HT.

Automatic Detection of PS and Mechanical Filaments in the Ventricular Wall.

PS were automatically detected by first computing the phase angle of the HT of the reconstructed and bandpass filtered data (SI Appendix, Fig. S9 and Note 8). The gradients of the phase angles along x and y were calculated and unwrapped between $-\pi$ and $+\pi$. The line integral (i.e., curl of the unwrapped gradient vectors along the x and y directions) was then computed. As previously reported, mechanical strain waves emerging from electrical stimulation site, and the PS generally coincide with the electrode positions on the heart (20). Herein, we only considered PS with the highest curl value in the close proximity of the electrical stimulation site, thus excluding PS occurring in the nonarrhythmic regions of the heart. Mechanical filaments within the ventricular wall of the murine heart were reconstructed by connecting between the PS detected in different slices of the 3D image stack.

Data Availability. All study data are included in the article and/or supporting information.

ACKNOWLEDGMENTS This research was supported in part by the European Research Council under Grant Agreement No. ERC-CoG 2015-682379. We thank Dr. J. Christoph for his valuable inputs on physiological interpretation of the data. We also thank P. Kohl, C. Zgierski-Johnston, and F. Schneider-Warme for helpful discussions. Guidance from H.-C. A. Lin and V. Schötle on the Langendorff experiments is greatly appreciated.

1. T. Lewis, Report CXIX. Auricular fibrillation: A common clinical condition. *BMJ* **2**, 1528 (1909).
2. A. P. Landstrom, D. Dobrev, X. H. T. Wehrens, Calcium signaling and cardiac arrhythmias. *Circ. Res.* **120**, 1969–1993 (2017).
3. R. Peyronnet, J. M. Nerbonne, P. Kohl, Cardiac mechano-gated ion channels and arrhythmias. *Circ. Res.* **118**, 311–329 (2016).
4. G. Tse, Mechanisms of cardiac arrhythmias. *J. Arrhythm.* **32**, 75–81 (2016).
5. H. Cochet *et al.*, Cardiac arrhythmias: Multimodal assessment integrating body surface ECG mapping into cardiac imaging. *Radiology* **271**, 239–247 (2014).
6. M. J. M. Cluitmans *et al.*, In vivo validation of electrocardiographic imaging. *JACC Clin. Electrophysiol.* **3**, 232–242 (2017).
7. C. Ramanathan, R. N. Ghanem, P. Jia, K. Ryu, Y. Rudy, Noninvasive electrocardiographic imaging for cardiac electrophysiology and arrhythmia. *Nat. Med.* **10**, 422–428 (2004).
8. C. B. Higgins, A. de Roos, *MRI and CT of the Cardiovascular System* (Lippincott Williams & Wilkins, 2006).
9. T. A. Roberts *et al.*, Fetal whole heart blood flow imaging using 4D cine MRI. *Nat. Commun.* **11**, 1–13 (2020).
10. K. Nieman, S. Balla, Dynamic CT myocardial perfusion imaging. *J. Cardiovasc. Comput. Tomogr.* **14**, 303–306 (2020).
11. A. Pullan, M. L. Buist, L. K. Cheng, *Mathematically Modelling the Electrical Activity of the Heart: From Cell to Body Surface and Back Again* (World Scientific Publishing Company, 2005).
12. H. J. Vos *et al.*, Cardiac shear wave velocity detection in the porcine heart. *Ultrasound Med. Biol.* **43**, 753–764 (2017).
13. J. Provost, W.-N. Lee, K. Fujikura, E. E. Konofagou, Imaging the electro-mechanical activity of the heart in vivo. *Proc. Natl. Acad. Sci. U.S.A.* **108**, 8565–8570 (2011).
14. J. I. Laughner, F. S. Ng, M. S. Sulkin, R. M. Arthur, I. R. Efimov, Processing and analysis of cardiac optical mapping data obtained with potentiometric dyes. *Am. J. Physiol. Heart Circ. Physiol.* **303**, H753–H765 (2012).
15. G. Salama, B. R. Choi, Images of action potential propagation in heart. *News Physiol. Sci.* **15**, 33–41 (2000).
16. C. Omichi *et al.*, Intracellular Ca dynamics in ventricular fibrillation. *Am. J. Physiol. Heart Circ. Physiol.* **286**, H1836–H1844 (2004).
17. B. R. Choi, G. Salama, Simultaneous maps of optical action potentials and calcium transients in guinea-pig hearts: Mechanisms underlying concordant alternans. *J. Physiol.* **529**, 171–188 (2000).
18. I. R. Efimov, V. P. Nikolski, G. Salama, Optical imaging of the heart. *Circ. Res.* **95**, 21–33 (2004).

19. T. J. Herron, P. Lee, J. Jalife, Optical imaging of voltage and calcium in cardiac cells & tissues. *Circ. Res.* **110**, 609–623 (2012).
20. J. Christoph *et al.*, Electromechanical vortex filaments during cardiac fibrillation. *Nature* **555**, 667–672 (2018).
21. J. Provost *et al.*, Simultaneous positron emission tomography and ultrafast ultrasound for hybrid molecular, anatomical and functional imaging. *Nat. Biomed. Eng.* **2**, 85–94 (2018).
22. B. Heiles *et al.*, Ultrafast 3D ultrasound localization microscopy using a 32×32 matrix array. *IEEE Trans. Med. Imaging* **38**, 2005–2015 (2019).
23. V. Lev-Ram, A. Grinvald, Ca^{2+} - and K^{+} -dependent communication between central nervous system myelinated axons and oligodendrocytes revealed by voltage-sensitive dyes. *Proc. Natl. Acad. Sci. U.S.A.* **83**, 6651–6655 (1986).
24. C. O’Shea *et al.*, High-throughput analysis of optical mapping data using ElectroMap. *J. Vis. Exp.* **148**, e59663 (2019).
25. S. Gigan, Optical microscopy aims deep. *Nat. Photonics* **11**, 14–16 (2017).
26. A. Taruttis, V. Ntziachristos, Advances in real-time multispectral optoacoustic imaging and its applications. *Nat. Photonics* **9**, 219–227 (2015).
27. I. R. Efimov, T. N. Mazgalev, High-resolution, three-dimensional fluorescent imaging reveals multilayer conduction pattern in the atrioventricular node. *Circulation* **98**, 54–57 (1998).
28. V. Kappadan *et al.*, High-resolution optical measurement of cardiac restitution, contraction, and fibrillation dynamics in beating vs. blebbistatin-uncoupled isolated rabbit hearts. *Front. Physiol.* **11**, 464 (2020).
29. J. Christoph, S. Luther, Marker-free tracking for motion artifact compensation and deformation measurements in optical mapping videos of contracting hearts. *Front. Physiol.* **9**, 1483 (2018).
30. P. Schaffer, H. Ahammer, W. Müller, B. Koidl, H. Windisch, Di-4-ANEPPS causes photodynamic damage to isolated cardiomyocytes. *Pflügers Arch.* **426**, 548–551 (1994).
31. A. Matiukas *et al.*, Near-infrared voltage-sensitive fluorescent dyes optimized for optical mapping in blood-perfused myocardium. *Heart Rhythm* **4**, 1441–1451 (2007).
32. A. P. Larsen, K. J. Sciuto, A. P. Moreno, S. Poelzing, The voltage-sensitive dye di-4-ANEPPS slows conduction velocity in isolated guinea pig hearts. *Heart Rhythm* **9**, 1493–1500 (2012).
33. L. Li *et al.*, Single-impulse panoramic photoacoustic computed tomography of small-animal whole-body dynamics at high spatiotemporal resolution. *Nat. Biomed. Eng.* **1**, 1–11 (2017).
34. X. L. Deán-Ben, T. F. Fehm, S. J. Ford, S. Gottschalk, D. Razansky, Spiral volumetric optoacoustic tomography visualizes multi-scale dynamics in mice. *Light Sci. Appl.* **6**, e16247 (2017).
35. A. Ron, X. L. Deán-Ben, S. Gottschalk, D. Razansky, Volumetric optoacoustic imaging unveils high-resolution patterns of acute and cyclic hypoxia in a murine model of breast cancer. *Cancer Res.* **79**, 4767–4775 (2019).
36. H. A. Lin *et al.*, Ultrafast volumetric optoacoustic imaging of whole isolated beating mouse heart. *Sci. Rep.* **8**, 14132 (2018).
37. H. A. Lin *et al.*, Characterization of cardiac dynamics in an acute myocardial infarction model by four-dimensional optoacoustic and magnetic resonance imaging. *Theranostics* **7**, 4470–4479 (2017).
38. I. Ivankovic *et al.*, Volumetric optoacoustic tomography enables non-invasive in vivo characterization of impaired heart function in hypoxic conditions. *Sci. Rep.* **9**, 8369 (2019).
39. I. Ivankovic *et al.*, Volumetric optoacoustic tomography differentiates myocardial remodelling. *Mol. Imaging Biol.* **22**, 1235–1243 (2020).
40. A. Özbek, X. L. Deán-Ben, D. Razansky, Optoacoustic imaging at kilohertz volumetric frame rates. *Optica* **5**, 857–863 (2018).
41. B. Mc Larney *et al.*, Uniform light delivery in volumetric optoacoustic tomography. *J. Biophotonics* **12**, e201800387 (2019).
42. D. Lang, M. Sulkin, Q. Lou, I. R. Efimov, Optical mapping of action potentials and calcium transients in the mouse heart. *J. Vis. Exp.* **55**, e3275 (2011).
43. I. Codreanu *et al.*, Longitudinally and circumferentially directed movements of the left ventricle studied by cardiovascular magnetic resonance phase contrast velocity mapping. *J. Cardiovasc. Magn. Reson.* **12**, 48 (2010).
44. E. E. Konofagou *et al.*, Noninvasive electromechanical wave imaging and conduction-relevant velocity estimation in vivo. *Ultrasonics* **50**, 208–215 (2010).
45. P. E. Dilaveris, J. E. Gialafos, P-wave dispersion: A novel predictor of paroxysmal atrial fibrillation. *Ann. Noninvasive Electrocardiol.* **6**, 159–165 (2001).
46. S. B. Knisley, N. Trayanova, F. Aguel, Roles of electric field and fiber structure in cardiac electric stimulation. *Biophys. J.* **77**, 1404–1417 (1999).
47. K. Umapathy *et al.*, Phase mapping of cardiac fibrillation. *Circ. Arrhythm. Electrophysiol.* **3**, 105–114 (2010).
48. S. F. Noujaim *et al.*, Universal scaling law of electrical turbulence in the mammalian heart. *Proc. Natl. Acad. Sci. U.S.A.* **104**, 20985–20989 (2007).
49. D. Vaidya, G. E. Morley, F. H. Samie, J. Jalife, Reentry and fibrillation in the mouse heart: A challenge to the critical mass hypothesis. *Circ. Res.* **85**, 174–181 (1999).
50. M.-H. Lee *et al.*, Patterns of wave break during ventricular fibrillation in isolated swine right ventricle. *Am. J. Physiol. Heart Circ. Physiol.* **281**, H253–H265 (2001).
51. J. Jalife, R. Gray, Drifting vortices of electrical waves underlie ventricular fibrillation in the rabbit heart. *Acta Physiol. Scand.* **157**, 123–131 (1996).
52. A. M. Tabrizi *et al.*, Spatiotemporal organization of electromechanical phase singularities during high-frequency cardiac arrhythmias. *arXiv [Preprint]* (2021). <https://arxiv.org/abs/2107.09223v2> (Accessed 22 July 2021).
53. X. L. Deán-Ben, D. Razansky, On the link between the speckle free nature of optoacoustics and visibility of structures in limited-view tomography. *Photoacoustics* **4**, 133–140 (2016).
54. H. Chen, T. Varghese, P. S. Rahko, J. A. Zagzebski, Ultrasound frame rate requirements for cardiac elastography: Experimental and in vivo results. *Ultrasonics* **49**, 98–111 (2009).
55. E. Konofagou *et al.*, Non-invasive systems and methods for rendering of cardiac electromechanical activation. U.S. Patent Application No. 16/572,328 (2020).
56. M. Schloegl, M. Holler, A. Schwarzl, K. Bredies, R. Stollberger, Infimal convolution of total generalized variation functionals for dynamic MRI. *Magn. Reson. Med.* **78**, 142–155 (2017).
57. M. Strachinaru *et al.*, Cardiac shear wave elastography using a clinical ultrasound system. *Ultrasound Med. Biol.* **43**, 1596–1606 (2017).
58. P. Song *et al.*, Quantitative assessment of left ventricular diastolic stiffness using cardiac shear wave elastography: A pilot study. *J. Ultrasound Med.* **35**, 1419–1427 (2016).
59. N. F. Otani, S. Luther, R. Singh, R. F. Gilmour Jr., Transmural ultrasound-based visualization of patterns of action potential wave propagation in cardiac tissue. *Ann. Biomed. Eng.* **38**, 3112–3123 (2010).
60. J. R. Leisey, D. A. Scott, L. W. Grotyohann, R. C. Scaduto Jr., Quantitation of myoglobin saturation in the perfused heart using myoglobin as an optical inner filter. *Am. J. Physiol.* **267**, H645–H653 (1994).
61. X. L. Deán-Ben, S. Gottschalk, B. Mc Larney, S. Shoham, D. Razansky, Advanced optoacoustic methods for multiscale imaging of in vivo dynamics. *Chem. Soc. Rev.* **46**, 2158–2198 (2017).
62. X. L. Deán-Ben *et al.*, Functional optoacoustic neuro-tomography for scalable whole-brain monitoring of calcium indicators. *Light Sci. Appl.* **5**, e16201 (2016).
63. S. Gottschalk *et al.*, Rapid volumetric optoacoustic imaging of neural dynamics across the mouse brain. *Nat. Biomed. Eng.* **3**, 392–401 (2019).
64. O. Degtyaruk, B. Mc Larney, X. L. Deán-Ben, S. Shoham, D. Razansky, Optoacoustic calcium imaging of deep brain activity in an intracardially perfused mouse brain model. *Photonics* **6**, 67 (2019).
65. L. Ding, X. L. Deán-Ben, D. Razansky, Efficient 3-D model-based reconstruction scheme for arbitrary optoacoustic acquisition geometries. *IEEE Trans. Med. Imaging* **36**, 1858–1867 (2017).
66. A. Beck, M. Teboulle, A fast iterative shrinkage-thresholding algorithm for linear inverse problems. *SIAM J. Imaging Sci.* **2**, 183–202 (2009).
67. M. Schmidt, N. L. Roux, F. R. Bach, “Convergence rates of inexact proximal-gradient methods for convex optimization” in *Advances in Neural Information Processing Systems 24 (NIPS 2011)* (NIPS, 2011), pp. 1458–1466.
68. A. Chambolle, T. Pock, A first-order primal-dual algorithm for convex problems with applications to imaging. *J. Math. Imaging Vis.* **40**, 120–145 (2011).
69. L. Clasen *et al.*, A modified approach for programmed electrical stimulation in mice: Inducibility of ventricular arrhythmias. *PLoS One* **13**, e0201910 (2018).
70. T. Bruegmann *et al.*, Optogenetic defibrillation terminates ventricular arrhythmia in mouse hearts and human simulations. *J. Clin. Invest.* **126**, 3894–3904 (2016).
71. M. R. Franz, Current status of monophasic action potential recording: Theories, measurements and interpretations. *Cardiovasc. Res.* **41**, 25–40 (1999).
72. M. Yokokawa *et al.*, Effect of linear ablation on spectral components of atrial fibrillation. *Heart Rhythm* **7**, 1732–1737 (2010).
73. R. Latchamsetty, A. G. Kocheril, Review of dominant frequency analysis in atrial fibrillation. *J. Atr. Fibrillation* **2**, 204 (2009).
74. S. Kaese, S. Verheule, Cardiac electrophysiology in mice: A matter of size. *Front. Physiol.* **3**, 345 (2012).
75. M. Rodrigo *et al.*, Body surface localization of left and right atrial high-frequency rotors in atrial fibrillation patients: A clinical-computational study. *Heart Rhythm* **11**, 1584–1591 (2014).